Rotating radial injection pattern for highly sensitive electrical impedance tomography of human lung anomalies

IOP Publishing Physiol. Meas. 13 (2025) 025001 https://doi.org/10.1088/1361-6579/ada9c2

Physiological Measurement

IPEM Institute of Physics and Engineering in Medicine

OPEN ACCESS

RECEIVED
27 September 2024

REVISED
28 November 2024

ACCEPTED FOR PUBLICATION
13 January 2025

PUBLISHED
6 February 2025

PAPER

Rotating radial injection pattern for highly sensitive electrical impedance tomography of human lung anomalies

Oumaima Bader[1,2], **Najoua Essoukri Ben Amara**[2], **Oliver G Ernst**[3] and **Olfa Kanoun**[1,*]

[1] Professorship of Measurement and Sensor Technology, Technische Universität Chemnitz, 09111 Chemnitz, Germany
[2] Université de Sousse, Ecole Nationale d'Ingénieurs de Sousse, LATIS—Laboratory of Advanced Technology and Intelligent Systems, Sousse 4023, Tunisia
[3] Department of Mathematics, Technische Universität Chemnitz, 09111 Chemnitz, Germany
[*] Author to whom any correspondence should be addressed.

E-mail: olfa.kanoun@etit.tu-chemnitz.de

Keywords: 3D modeling, EIT, finite element analysis, finite element method

Abstract

Objective. Electrical impedance tomography (EIT) is a non-invasive technique used for lung imaging. A significant challenge in EIT is reconstructing images of deeper thoracic regions due to the low sensitivity of boundary voltages to internal conductivity variations. The current injection pattern is decisive as it influences the current path, boundary voltages, and their sensitivity to tissue changes. *Approach.* This study introduces a novel current injection pattern with radially placed electrodes excited in a rotating radial pattern. The effectiveness of the proposed pattern was investigated using a 3D computational model that mimics the human thorax, replicating its geometry and tissue electrical properties. To examine the detection of lung anomalies, models representing both healthy and unhealthy states, including cancer-like anomalies in three different positions, were developed. The new pattern was compared to common patterns—adjacent, skip 1, and opposite—using finite element analysis. The comparison focused on the current density within lung nodules and the sensitivity to changes in anomaly positions. *Main results.* Results showed that the new pattern achieved the maximum current density within anomalies compared to surrounding tissues, with peak values near the closest electrode pairs to the anomalies. Specifically, current density magnitudes reached $72.73 \cdot 10^{-9}\,\mathrm{A \cdot m}$, $145.24 \cdot 10^{-9}\,\mathrm{A \cdot m}$, and $26.43 \cdot 10^{-9}\,\mathrm{A \cdot m}$ for the three different positions, respectively. Furthermore, the novel pattern's sensitivity to anomaly position changes surpassed the common patterns. *Significance.* These results demonstrate the efficiency of the proposed injection pattern in detecting lung anomalies compared to the common injection patterns.

1. Introduction

Electrical impedance tomography (EIT) is a non-invasive imaging technique that uses measurements with electrodes around a device under test to produce 2D images of internal electrical conductivity (Haddad *et al* 2021). One of the challenges which can be met by EIT is the early detection of lung cancer tissues. Lung cancer is a severe and widespread malignancy. Studies indicate that it became a leading cause of mortality within the European population in 2019 (Malvezzi *et al* 2019). For this reason, early detection without the need for computed tomography (CT) scans and continuous monitoring, like in the case of EIT, is very important. EIT measurements consist of applying an alternating current to two selected excitation electrodes and measuring the resulting potential at pairs of the remaining electrodes following a certain pattern. In most cases, the so-called *adjacent pattern* is employed, in which the excitation is successively provided by pairs of neighboring electrodes around the thorax (Putensen *et al* 2019), and the voltage measurements are carried out at neighboring pairs of measurement electrodes. The main limitation of this pattern is that it captures changes in conductivity mainly near the device under test (DUT) boundary, resulting in lower sensitivity for detecting changes within the DUT interior (Adler *et al* 2011, Putensen *et al* 2019). A second

common pattern is the *opposite* injection pattern, also called the *pseudo-polar* pattern, where the current injection is on pairs of electrodes on opposite sides. This pattern is more sensitive to changes in the central area of the thorax (Zhang *et al* 2020). A third common pattern is the *Skip N* pattern, with *N* a variable number of non-injection electrodes lying between the electrode excitation pair. In Rapin *et al* (2018), the Skip-5 pattern has been applied for the wearable EIT system. In Zhang *et al* (2020), it is shown that, for a larger number of skipped electrodes, a higher sensitivity can be realized. The Skip pattern has been applied in Putensen *et al* (2019) to increase the inter-electrode distance in 32-electrode systems. Further details on the injection principles of common injection patterns are given in section 3.2.

Numerous investigations have explored the impact of current injection methods and voltage measurement protocols on current density and measurement sensitivity to enhance the quality of EIT images (Brown and Segar 1987, Avis and Barber 1994, Kauppinen *et al* 2006, Zhang and Wang 2010, Adler *et al* 2011). Deep investigations of optimal EIT injection patterns are provided in Lionheart *et al* (2001), Demidenko *et al* (2005), Dang *et al* (2021). In Dang *et al* (2021) four injection patterns for EIT—adjacent, opposite, full-scan, and trigonometric—were compared based on reconstructed image quality for a circular EIT DUT, concluding that the full-scan and trigonometric patterns produce the most accurate images but require more complex measurement systems and longer acquisition times compared to the adjacent and opposite patterns. In (Demidenko *et al* 2005), Eugene *et al* developed a statistical criterion for optimal current or voltage patterns in planar circular EIT DUT and found that the optimal voltage pattern for conductivity estimation is the cosine pattern. The discussion of safety constraints, in terms of maximum ohmic power, to determine the optimal current pattern in Lionheart *et al* (2001) represents an advancement in EIT technology for safer imaging protocols.

In this work, we systematically investigate the impact of current injection patterns on detecting local anomalies in human lung tissue, referred to as *nodules*. The selection and investigation of the measurement protocol are expected to have a significant impact on the EIT measurement data set and image quality. In this paper, we explore the impact of the current pattern on lung nodule detection based on the current density by numerical methods. For this, we develop a realistic 3D thorax model based on the segmentation of a series of medical images to approximate the outer surface as well as the internal boundaries of different conductivity regions. The resulting high-fidelity geometric model allows for a realistic simulation of the current distributions. A careful mesh convergence study ensures a sufficiently accurate approximation quality for the numerical model employed for the simulations. For quantitative assessment, we propose metrics relying on the analysis of current density, electrical potential, and sensitivity to changes in nodule position. Thereby, the objective is to streamline the evaluation process, particularly in identifying the most effective injection pattern for nodule detection.

The paper is structured in five sections: section 2 provides a comprehensive overview of existing human thorax models, establishing the foundation for the study. Section 3 provides the details of the constructed geometric model and numerical simulation environment, detailing the mesh assessment, the proposed current injection pattern, and the evaluation metrics used. Section 4 presents the results of a comparative study, analyzing common current injection patterns with the proposed injection pattern in both healthy and unhealthy lung scenarios. Section 4 interprets these results, offering detailed insights into the effectiveness of the proposed method. Finally, we conclude the study and provide an outlook in section 5.

2. Finite element human thorax models

For EIT imaging, realistic and quite complex geometrical human thorax modeling is crucial to enhance the precision of parameter prediction, and it has seen significant advancements in recent studies (Wu *et al* 2006, Fan and Wang 2010, Menden *et al* 2018, Li *et al* 2019, Zhang *et al* 2020, Huang *et al* 2021, Dussel *et al* 2022). In Zhang *et al* (2020), a 3D geometric model is developed that includes the lungs, heart, and thoracic cavity, where the latter is modeled as a layer of fat scaled to simulate the effects of different obesity levels on EIT measurements. Different injection patterns are compared, such as the adjacent, Skip N with $N \in \{1, \ldots, 7\}$, based on the resolution of the reconstructed images and the boundary voltages. The 3D FE model developed in Zhang *et al* (2020) is not subjected to any evaluation or optimization of mesh convergence to obtain the optimal EIT solution, which is considered a limitation since the resolution of the reconstructed images for the assessment is affected directly by the mesh parameters. In Fan and Wang (2010), a 3D human thorax geometry is proposed to simulate human lung ventilation by segmenting sequential CT scan images as input to the algorithm. The resulting model contains an extensive number of nodes leading to a non-smooth thorax geometry. In addition, an FE mesh convergence study is not elaborated which leads to numerical calculation inaccuracy. In Wu *et al* (2006), a cylindrical geometry is used to investigate the effect of different breathing stages on the resulting impedance. The limitation of such a model is the inaccuracy of the evaluation due to limited shape fidelity. In Menden *et al* (2018), CT scans are also used to reconstruct the geometry. Thus, this

Table 1. Comparative table of the developed 3D FE models of the thorax for numerical analysis.

Paper	Method	FE Mesh	Organs	Mesh convergence	Injection pattern
Zhang *et al* (2020)	Not mentioned	Not mentioned	Heart, lungs and fat	No	Adjacent Skip N N (1,..,7)
Fan and Wang (2010)	CT scans segmentation	54 185 tetrahedral elements	Heart, lungs and body fluid	No	Adjacent
Menden *et al* (2018)	Visible images	52 570 triangular elements	Heart, lungs and muscle	No	Skip 4
Dussel *et al* (2022)	Camera images	Triangular and tetrahedral elements	Thorax cavity	No	—
Huang *et al* (2021)	22 MRI images	9953 nodes	lungs and muscle	No	Adjacent
Li *et al* (2019)	CT scans segmentation	70 667 tetrahedral elements	Lungs and body fluid	No	Adjacent Skip 1,2 Opposite
Ma *et al* (2023)	CT scans segmentation	45 917 tetrahedral elements	Thorax cavity lungs, heart	No	Adjacent
This work	CT scans segmentation	Free tetrahedral: 623 124 elements for healthy model	Skin, fat, muscle, lungs, heart, and cancer and 641 824 for unhealthy model	Yes	Adjacent Skip 1 Opposite Rotating Radial

process is time-consuming for large CT data sets. In Dussel *et al* (2022), the data is acquired directly using a camera, that extracts features directly from the body using a video recording pipeline. Therefore, video instability errors and variations in the distance lead to geometry inaccuracy. In Huang *et al* (2021), magnetic resonance imaging (MRI) scans are converted to grayscale and segmented. However, this approach does not operate efficiently with flat images or those without peaks. Moreover, since it considers only the image's grayscale information with no additional structural information, it is sensitive to grayscale irregularities and noise. In Li *et al* (2019), CT data has been filtered for geometry design. Due to the instability of the average variance of the employed filter, the corresponding output presents a poor level of binarization. In Ma *et al* (2023), the 3D model generation is based on a series of 2D transverse planar CT scans of the human body taken at different longitudinal positions. The scans are taken from a standard-sized male individual, and the data are recorded during the end-inspiration breath hold while lying in the supine position. The resulting model geometry in Ma *et al* (2023) is non-smooth, which leads to unreliable numerical results.

The comparison in table 1 Shows that the previously mentioned papers that elaborated on FE models for numerical analysis did not assess FE mesh quality or the convergence of the forward calculation. This is a critical oversight, as mesh quality, including element size, shape, and distribution, can significantly affect the convergence and accuracy of the FE approximation results, and evaluating the convergence of the forward calculation is essential to ensure the reliability and accuracy of the numerical results. Without these crucial assessments, the studies provide an incomplete understanding of the FE modeling and analysis process, as the impact of mesh quality and convergence of the forward calculation is not addressed.

In contrast to the previously discussed papers, we here design a refined and smoothed 3D FE human thorax model which is then employed in the numerical simulation of the EIT response. The importance of geometric model fidelity in simulating real-world scenarios is crucial, resulting from the accurate pre-processing of the model to ensure its robustness. Additionally, a mesh convergence study is incorporated into the investigation to determine optimal mesh parameters.

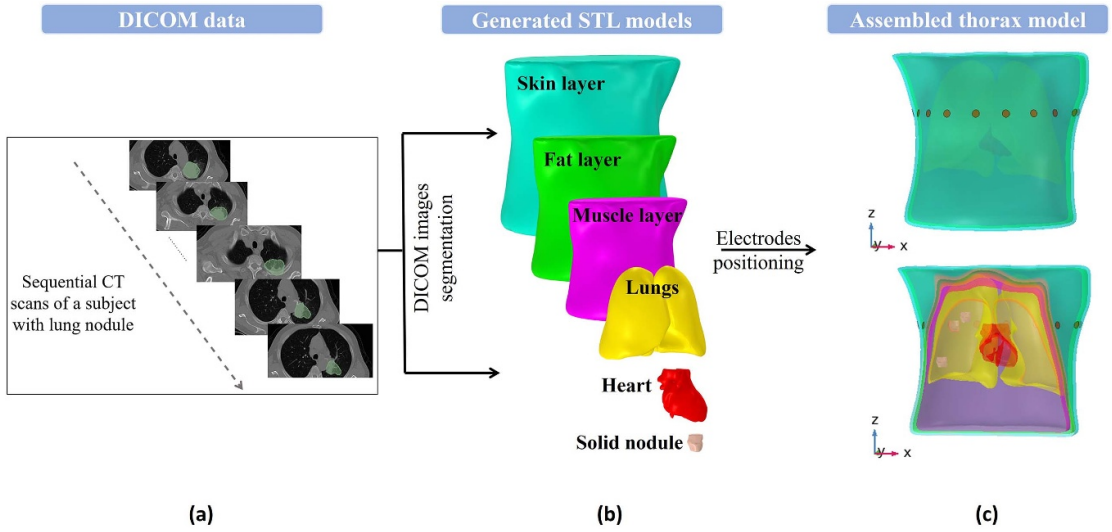

Figure 1. Realistic geometry design of the human thorax: (a) DICOM data used for models generation, (b) generated STL models of the skin, fat, muscle, heart, lungs, and lung nodule (c) human thorax model.

3. Methodology

3.1. Human thorax model design

Creating an accurate geometric model for EIT computations involves careful attention to both shape and electrical properties to ensure precise results. This is crucial because it greatly affects how electrical currents flow and how impedance distribution is subsequently reconstructed. Additionally, accurate electrical characteristics conductivity σ and relative permittivity ε_r, must be assigned to different regions within the geometry. To design the model, we apply a combination of image segmentation techniques and computational modeling methodologies. High-resolution CT scans are used to acquire detailed 3D data of the chest region. The model is based on 87 sections of CT images of a 25-year-old male, presented as digital imaging and communications in medicine (DICOM) files (DICOM Library 2024). The CT data obtained is subsequently processed and transformed using 3D Slicer software (Fedorov *et al* 2012). The model generation procedure involves choosing functions for geometry, outlining a contour line, and refining intricate regions. Once the suitable area is selected, the surface rendering technique is employed. This technique relies on a contour tracing algorithm that analyzes the pixels of segmented regions, ultimately producing a cluster of dots linked to each point assigned to the corresponding pixel in 3D space. These algorithms aided in precisely isolating and outlining the various anatomical structures within the human chest, including the lungs, heart, and soft tissues. The generated models for different thorax subregions are later assembled using the mesh resemblance algorithm. As a result of the assembly operation, an STL (stereolithography file) is generated with a volume of 41.36 cm as length, 31.79 cm as width, and 36.51 as height. To simulate EIT excitation and measurement, circular electrodes with a diameter of 1.5 cm are placed 7.3 cm apart around the exterior of the human chest model in the usual horizontal plane arrangement at a distance of 12.51 cm from the top of the thorax model. The electrode plane corresponds to the 4th to 5th intercostal spaces (ICS) at the parasternal section (Tomicic and Cornejo 2019). The final 3D human chest model is composed of skin, fat, muscle, heart, and lung regions with 16 in-plane electrodes to perform AC injection and potential measurement. The complete thorax model is shown in figure 1.

In this work, we consider a series of lung nodules as a case study for anomalies in lung composition. For the nodule segmentation, another integrated dataset consisting of 92 CT sequential DICOM images deriving from a 58-year-old male, with lung nodules in different stages, was used to design the inhomogeneities. The nodule is located in the upper part of the right lung as demonstrated in figure 1. The resulting models of tumor tissue—the nodules—are shown in figure 1. The segmented nodule will be integrated into the healthy lung model at three different locations in the right lung, as shown in figure 2, to mimic unhealthy lung tissue and to study the effects of the current patterns on its detectability. Our study is accomplished in three distinct steps. Initially, a realistic geometry is constructed to mimic the anatomical features of the human thoracic region. Then, a realistic geometry of lung nodules is designed to describe lung nodule tissue. The final step consists of a series of FE EIT forward simulations, followed by an evaluation metric and sensitivity analysis performed to investigate optimal current injection patterns and to investigate a specific newly proposed

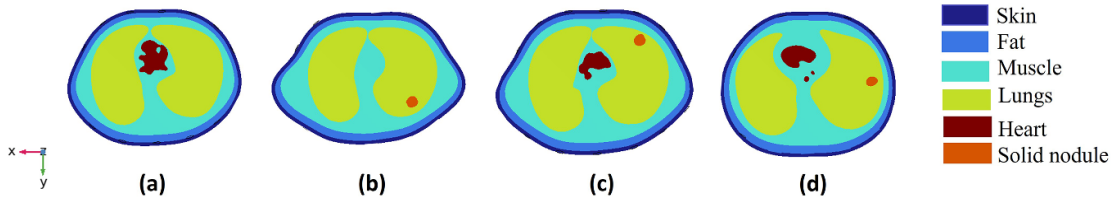

Figure 2. Dorsal orientation: (a) healthy lung model in cross-section, lung nodule positions within the healthy lung in (b) case 1 (c) case 2 (d) case 3.

Table 2. Dielectric properties of model tissue types at $f = 50$ kHz according to Bader *et al* (2021, 2022), Wang *et al* (2022).

Model part	Conductivity σ (S m^{-1})	Relative permittivity ε_r
Lungs	0.27	98.56
Skin	0.000 27	1126.80
Fat	0.02	172.42
Heart	0.195 43	16 982
Muscle	0.35	10 094
Nodule (lung anomaly)	0.5	10^3
Ag/AgCl electrodes	10^5	3.5

pattern for efficient anomaly detection. Figure 2 represents an overview of the cases investigated by the numerical simulation in this study. Besides the subdomain boundaries of the different thoracic regions, the (isotropic) electrical properties of the occurring tissue types are required for the simulation. These are taken from the literature and given in table 2 for an AC frequency of $f = 50$ kHz.

3.2. Finite element simulation

We employ FE approximation to simulate the EIT forward model, i.e. excitation and measurement, to investigate the effectiveness of different current injection patterns for nodule detection. To assess the robustness of the simulation, a Gaussian white Noise with a *Signal to Noise Ratio* (SNR) of 50 dB was added to the finite element analysis (FEA) (Zhou *et al* 2018). The mathematical model relating injection currents to potential values at measurement electrodes, approximated by FE discretization, is described below.

3.2.1. EIT boundary value problem

The standard model of the EIT forward problem follows from Maxwell's equations and consists of a stationary elliptic diffusion equation for the electric potential (see Borcea 2002 for a derivation). We assume the electrical properties of the different tissue types in the domain of interest Ω within the thorax to be piecewise constant as specified by the values in table 2. The resulting complex conductivity, also known as *admittivity* (*impedance* is its reciprocal),

$$\gamma = \gamma(\vec{x}, \omega) = \sigma + \mathrm{i}\omega\varepsilon_0\varepsilon_r, \qquad \mathrm{i} = \sqrt{-1}, \tag{1}$$

where $\omega = 2\pi f$ denotes the angular frequency of the applied time-harmonic electric current and ε_0 the permittivity of free space, σ is the conductivity, and ε_r is the relative permittivity. Under the usual quasi-static approximation (see Adler and Holder 2021, chapter 5) at a fixed frequency ω in the absence of current sources or sinks inside Ω, the scalar electric potential $\phi = \phi(\vec{x})$, $\vec{x} = (x, y, z) \in \Omega$, satisfies the stationary diffusion equation

$$\nabla \cdot [\gamma \nabla \phi] = 0, \tag{2}$$

with a current density along the boundary $\partial\Omega$ given by

$$j_{\vec{n}} = j_{\vec{n}}(\vec{x}) = \vec{n} \cdot (\gamma \nabla \phi), \qquad \vec{x} \in \partial\Omega, \tag{3}$$

where $\vec{n}$ denotes the outward unit normal vector along $\partial\Omega$. Conservation of current requires the sum of all currents entering and leaving Ω to vanish so that $j_{\vec{n}}$ must satisfy the consistency condition

$$\int_{\partial\Omega} j_{\vec{n}} \, \mathrm{d}S = 0, \tag{4}$$

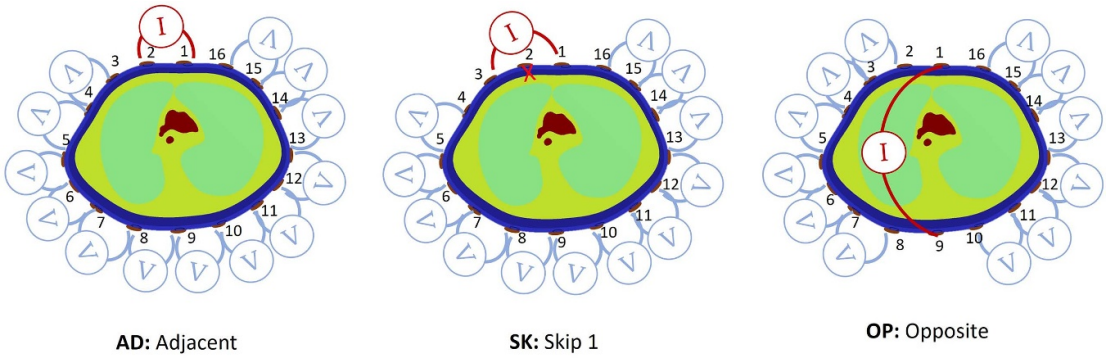

Figure 3. AD, SK, and OP current injection patterns with associated voltage difference measurements.

where dS denotes surface measure. Denoting the L disjoint boundary segments occupied by electrodes by $\mathcal{E} = \cup_{\ell=1}^{L} e_\ell$, the *shunt* model complements the diffusion equation (2) with the boundary conditions

$$j_{\vec{n}} = 0, \qquad \text{along } \partial\Omega \setminus \mathcal{E}, \tag{5a}$$

$$\int_{e_\ell} j_{\vec{n}} \mathrm{d}S = I_\ell, \qquad \ell = 1 \ldots L, \tag{5b}$$

$$j_{\vec{n}} \text{ constant on } e_\ell, \qquad \ell = 1 \ldots, L, \tag{5c}$$

where I_ℓ denotes the current applied at electrode e_ℓ. The more accurate *complete electrode model* (CEM) (Somersalo *et al* 1992), which accounts for both the shunting effect of the electrodes as well as the contact impedances between electrodes and tissue, replaces (5*c*) with

$$\phi + z_\ell j_{\vec{n}} = U_\ell \qquad \text{on } e_\ell,\ \ell = 1 \ldots, L, \tag{6}$$

where z_ℓ denotes the (constant) contact impedance at electrode e_ℓ and U_ℓ the potential (voltage) measured there. Existence and uniqueness of the EIT forward problem (conservation of charge and choice of ground) require the injected currents and measured voltages to satisfy

$$\sum_{\ell=1}^{L} I_\ell = \sum_{\ell=1}^{L} U_\ell = 0. \tag{7}$$

The complete EIT forward problem now consists of fixing the complex conductivities γ throughout Ω, the contact impedances z_ℓ at the electrodes, as well as the injected currents I_ℓ, which have opposite signs at the injection pair and are zero at the remaining electrodes, and numerically solving the resulting boundary value problem. The evaluation of the voltages U_ℓ at the non-injection electrodes constitute the simulated measurements associated with the given injection pair.

3.2.2. Common EIT current injection patterns

The choice of the current injection pattern is decisive for the resolution and quality of EIT measurements. In a first step to study and evaluate different EIT current injection patterns for imaging and anomaly detection, we present the results of FE forward simulation for the three common EIT patterns: *Adjacent* (AD), *Skip 1* (SK), and *Opposite* (OP), as depicted in figure 3. The AD pattern, by far the most commonly used in EIT for lung monitoring, is based on injecting a low current through two neighboring electrodes, measuring the voltage difference across all remaining electrode pairs, and then rotating this arrangement across all possible adjacent injection electrode pairs. The limitation of the AD pattern lies in its sensitivity to conductivity changes mainly near the electrode surface, posing challenges in detecting interior changes (Adler *et al* 2011, Putensen *et al* 2019). In the OP pattern, current is injected through two diametrically opposing electrodes. The benefit of employing such a pattern is its direct flow through the center of the measured medium. However, a drawback is that it entails only half as many measurement configurations as AD, leading to reduced data (Putensen *et al* 2019). In the SK pattern, one electrode is skipped in this case for every injection round. This pattern is mostly used to increase inter-injection-electrode spacing when a larger number of electrodes, say 32, are present (Putensen *et al* 2019). In each of these three patterns, the boundary voltage differences are measured across all remaining neighboring electrodes (cf figure 3).

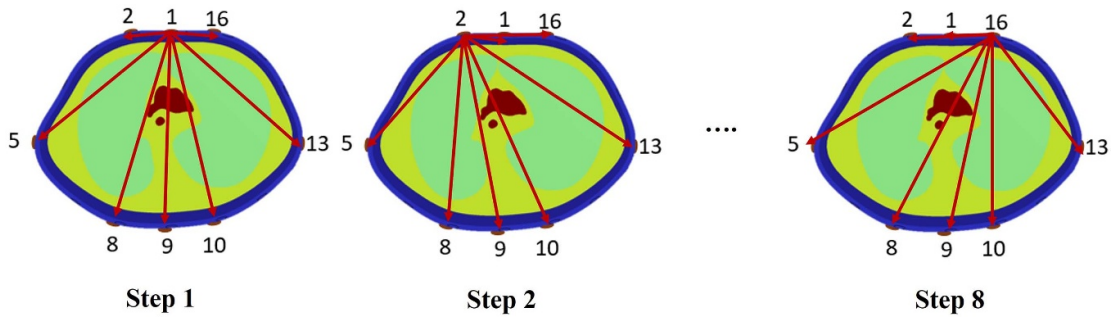

Figure 4. Eight steps of the proposed RR injection pattern with a cross-section of the FEM model.

Table 3. Parameters of the studied injection patterns in a 16-electrode EIT system (t is the time for one injection).

Pattern	AD	SK	OP	Full	RR
Number of excitation electrodes	16	16	16	16	**8**
Number of current injections	16	16	8	120	**28**
Number of voltage measurements	208	192	192	1170	**339**
Injection time	16 t	16 t	8 t	120 t	**28** t

3.2.3. Proposed rotating radial (RR) current injection pattern

In this paper, we propose a new injection pattern, called the RR, where a radial current injection is carried out with a rotating focal point on the boundary of the DUT. It aims to gain as much information as possible from a given set of electrodes by having more current paths compared to the common patterns. Noting that including measurements from Full possible injection electrode pairs will lead to high measurement times and data redundancies (Dang *et al* 2021), we propose an arrangement for 16-electrode settings which involves 8 electrodes, among which alternate injection pairs are chosen which are then rotated around the thorax to obtain a full data set. We propose to select the eight electrodes, so that three are chosen to be in front, near the heart and lungs starting from the sternum position as shown in figure 4. Three further electrodes are selected to be in the back near the largest lung region, and the remaining two are located to the left and right of the lungs. As it features arrangements from the AD, OP, and SK patterns, RR can be expected to combine the advantages of all three. For this set of electrodes, after eliminating reciprocal current paths, 28 possible current paths are measured, resulting in a total of 339 voltages. Supposing t is the time needed for one injection between one pair of electrodes, table 3 summarizes the total number of current injections and voltage measurements of the common patterns compared to the proposed RR pattern. The Full pattern represents all possible injection electrode pairs. Table 3 shows that the Full pattern utilizes 16 electrodes which necessitates 120 injections and 1170 measurements. However, our proposed RR pattern, which employs only eight electrodes, significantly lowers the injections to 28 paths and 339 voltage measurements. This pattern results in an estimated time reduction of approximately 76.7 %.

Figure 4 displays, within a cross-section of the FE model, the first measurement round of the proposed RR pattern in Step 1 involving, in turn, injection electrodes (1–2,1–5,1–8,1–9,1–10,1–13,1–16). The full measurement round then consists of all injection pairs in steps 1 through Step 8. Figure 5 displays the resulting current streamlines within the section of the FE model in the electrode plane. It shows the first 7 current paths resulting from the first round of injection. The chosen set of electrodes exhibits a noticeable current coverage over the different human thorax tissues, with a higher possibility that at least one path flows through a potential lung nodule. Furthermore, there are current injection paths at different angles. Injections 6 and 7 show a higher diffusion than injection 1, followed by the rest of the injections.

In the next step, the previously mentioned injection patterns will be evaluated in terms of current density from the electrodes through the lungs and the lung nodule to investigate the effect of the injection pattern in the enhancement of anomaly detection, as well as the sensitivity to the nodule position changes. In the evaluation of the EIT current injection pattern for human thorax application, a crucial aspect lies in assessing the integral of the current density $J(\mathrm{A\ m^{-2}})$ within the lungs, and the anomaly tissues, to compare it to that within the surrounding skin, muscle, heart, and fat tissues. This analysis is essential as it yields valuable insights into the efficiency and precision of the RR pattern in thoracic anomaly detection. By measuring both the distribution and magnitude of current density, it becomes possible to ascertain the current penetration

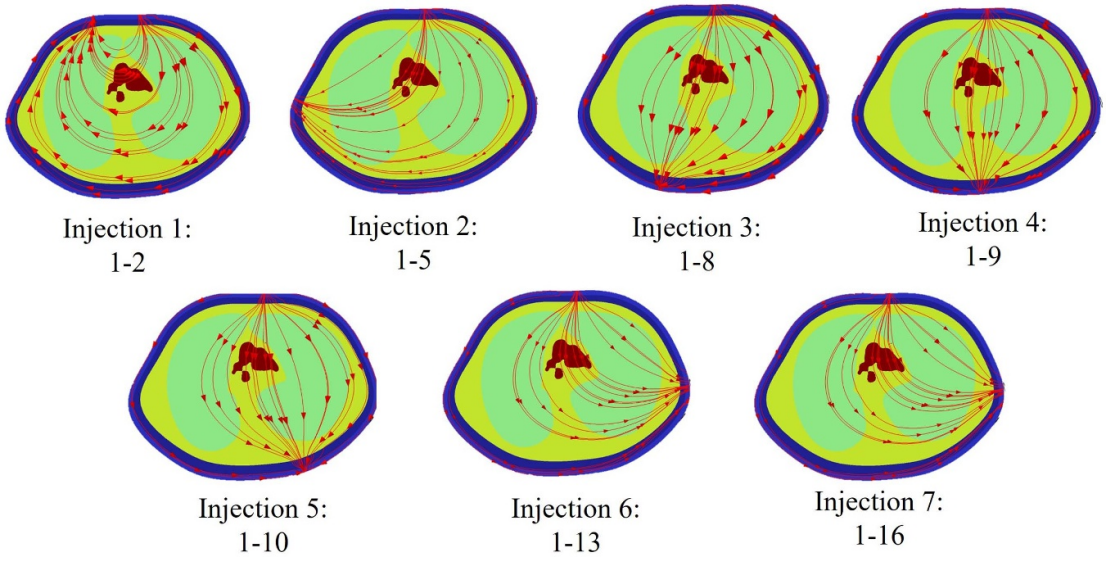

Figure 5. Current injections paths of step 1 using RR pattern: current streamline distribution within the electrode cross-section.

into the lungs. The current density is given in terms of the electric potential by Ohm's law

$$\vec{J} = -\gamma \nabla \phi, \qquad \gamma = \sigma + \mathrm{i}\omega\varepsilon_0\varepsilon_r. \tag{8}$$

As an indicator of current strength within a given subdomain such as the lung region Ω_L or the region Ω_A occupied by the anomaly, we consider

$$J_L := \int_{\Omega_L} \|\vec{J}\| \, \mathrm{d}\vec{x}, \quad \text{and} \quad J_A := \int_{\Omega_A} \|\vec{J}\| \, \mathrm{d}\vec{x}, \tag{9}$$

respectively, where $\|\cdot\|$ denotes the Euclidean norm. These integrals represent useful information for the detection of the anomaly within the lungs, as well as the evaluation of the most beneficial pattern.

3.3. Mesh generation and convergence

Once the 3D geometry, boundary conditions, and the current injection pattern have been defined, the next step in the FE forward simulation is the generation of a mesh with sufficient resolution. Mesh generation and subsequent FE computations are carried out in the COMSOL Multiphysics 6.1 environment using the 'Electric Currents (ec)' interface within the AC/DC module. We employ an unstructured tetrahedral mesh, which is particularly suited to model the complex 3D geometries occurring in our human thorax model. Obtaining an accurate FE solution requires generating a mesh that sufficiently resolves the different components of the thorax geometry. To determine the minimum number of elements needed for accurate meshing of the lung and nodule subdomains, a refinement of the mesh density is applied, and the convergence of the current density is monitored. For this purpose, and to simplify the mesh monitoring process, the AD, SK, OP, and RR current injection patterns are employed. Throughout the process, different levels of mesh refinement are applied while maintaining the pair of electrodes injecting the current. This approach involved increasing the mesh density by decreasing the size of the tetrahedral elements by way of the *physics-controlled mesh* feature in COMSOL Multiphysics, which allows for finer mesh resolution in different subdomains. The convergence of current density within the lungs and the nodule in its first position determines the optimal number of finite elements required. The element size was reduced and the meshes were created using the same settings to obtain the finest mesh containing 457 180 elements in the lung subdomain and 90 232 in the nodule subdomain. Then, the differences in simulated current density on these meshes were compared to the differences of the next coarser meshes, taking the finest mesh as a reference. Figure 6 shows the convergence of the relative error

$$e_{\mathrm{rel}} = \frac{\left| \int_{\Omega_D} \|\vec{J}_{\mathrm{coarse}}\| - \|\vec{J}_{\mathrm{fine}}\| \, \mathrm{d}\vec{x} \right|}{\int_{\Omega_D} \|\vec{J}_{\mathrm{fine}}\| \, \mathrm{d}\vec{x}}, \tag{10}$$

where Ω_D refers to either the lung subdomain Ω_L or the nodule subdomain Ω_A, which we use as indicators of solution accuracy to ascertain the required mesh density.

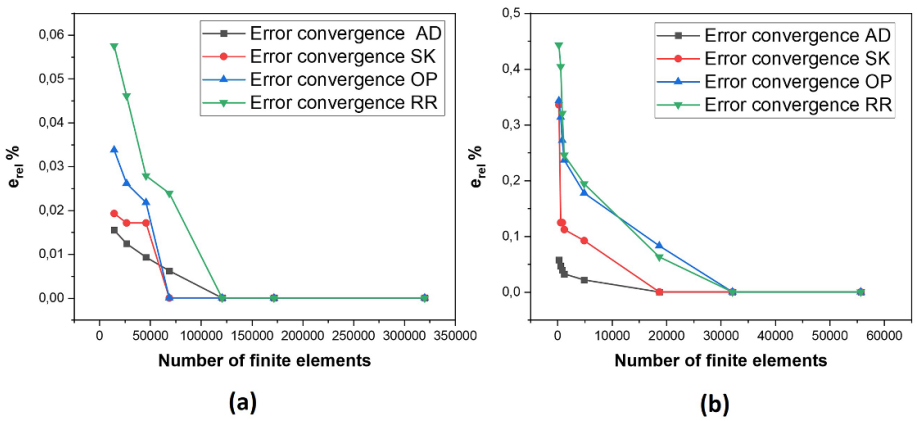

Figure 6. Convergence of relative error in aggregated subdomain current densities with mesh refinement using the finest mesh for reference: (a) lung subdomain (b) anomaly (nodule) subdomain.

Table 4. Evaluation of FE mesh quality metrics (Al-Abassi *et al* 2022).

Metric	Skewness	Growth rate	Condition number
Healthy lungs	0.45	0.7	0.5
Unhealthy lungs	0.44	0.69	0.6

Figure 6(a) shows the convergence of the relative error for a successively finer mesh, extending up to 320 148 elements for the lung subdomain. We observe a monotone error decrease with increasing mesh density for all four injection patterns, with initially more rapid convergence for the SK and OP patterns. Figure 6(b) presents the same results for the nodule subdomain, with up to 55 723 tetrahedra. Here, the convergence behavior is more pronounced, with the OP pattern exhibiting the highest initial error but achieving similar low error values as the AD and SK configurations at higher mesh densities. However, when a sufficiently fine resolution is achieved, the simulated relative error reaches essentially zero. This observation suggests that, beyond this specific resolution, further refinement will not improve solution accuracy. The mesh convergence study in figure 6 determined the optimal number of tetrahedral elements to achieve sufficiently accurate results for the current density integrals to be 120 789 for the lung mesh and 32 145 for the nodule mesh. This mesh density effectively balances accuracy with computational efficiency and time, ensuring accurate results while avoiding excessively long and heavy calculation duration. The results given below were all obtained using the optimal number of elements thus determined. This final model consists of a total mesh composed of 623 124 tetrahedra for the healthy lung model, each representing a discrete volume within the chest. Similarly, the unhealthy lung mesh is composed of 641 824 tetrahedral elements. The mesh generation time is reduced to 3 min (from 10 min for the reference mesh) using a computer with AMD Ryzen 9 5950X, 16-core processor, 3.40 GHz, and RAM of 128 GB.

In the second stage of mesh assessment, a thorough evaluation of mesh quality is conducted, taking into account essential features as outlined in table 4. This evaluation is conducted before proceeding with EIT simulations, as it is essential to ensure the accuracy and reliability of the results. Table 4 presents the optimal mesh quality features, predefined in COMSOL Multiphysics, such as the skewness, growth rate, and condition number, (Mesh Element Quality and Size 2024) (Al-Abassi *et al* 2022), which are obtained after refining and smoothing the model to facilitate the convergence of the FEM solver. These features should generally be less than 0.8 to avoid numerical errors and forward calculation inaccuracy (Mesh Element Quality and Size 2024). All the features are between 0.4 and 0.7, which is an acceptable range in our application. The final optimal mesh is represented in figure 7.

4. Results and discussion

Incorporating the detailed anatomical structure of the human thorax into the FEM-CEM simulation model enhances the reliability of EIT investigations. Analyzing the current density within the lungs and the nodule compared to adjacent tissues and the measured electrical potential within the electrodes assists in discerning potential undesired effects in future investigations. Utilizing a standard FE discretization for the EIT forward calculation results in a linear system that exhibits symmetry and positive definiteness, allowing for a solution via direct or iterative solvers. For our study, the COMSOL Multiphysics 6.1 framework is used for FEA. In

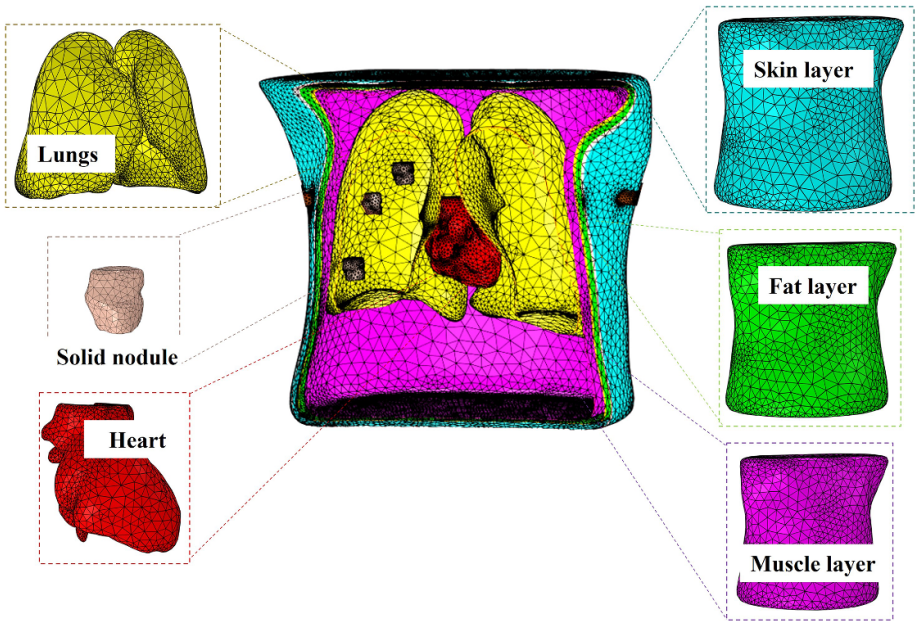

Figure 7. Generated tetrahedral FEM model: the mesh model is composed of the skin, fat, muscle, lungs, and heart, with insertion of the lung nodule in three different positions to be treated as separate cases.

this framework, both direct and iterative solvers are available for solving linear systems of equations. In our study, an iterative solver is used. An alternating low amplitude current of $I = 1$ mA, and frequency $f = 50$ kHz is applied to the 16 electrodes, as optimal AC signal properties for the human lung monitoring application (Tomicic and Cornejo 2019). The contact impedances are set to $z_l = 10^{-6}\,\Omega \cdot \mathrm{m}^2$, as an initial value for investigations, representing the value of Ag AgCl electrodes (Lee *et al* 2022). The next section will discuss the current density, electrical potential sensitivity, and the sensitivity to the nodule position.

4.1. Current density and electrical potential evaluation

Evaluating the current density is critical in optimizing the EIT current injection pattern, allowing for the refinement and advancement of EIT applications in thoracic imaging and physiological monitoring. Four scenarios corresponding to healthy lung and nodule cases 1, 2, and 3, respectively, are simulated by injecting the low AC through the attached electrodes of the FE models. As a first step, the proposed RR pattern is compared to the Full pattern to demonstrate the efficiency of the selected set of electrodes using the FE model. Figure 8 compares the current density J_L distribution within the lungs for the proposed RR injection pattern, which uses 8 electrodes, to the full, which involves 16 electrodes, in the context of healthy lungs. Despite the RR pattern utilizing fewer electrodes leading to fewer current injections, its current density values remain comparable to the full. This demonstrates that the RR pattern effectively preserves high current density within the lungs while reducing the number of electrodes and injections. As a result, the RR pattern offers a balance between measurement efficiency and sensitivity.

The same comparison was conducted within the anomaly region. Figure 9 represents the anomaly current densities J_A against the index of the current injection electrodes. Results demonstrate that the RR pattern effectively preserves high current density within the nodule while reducing the number of electrodes and injections. As a result of its demonstrated efficiency in maintaining comparable current density with fewer electrodes, the RR pattern is chosen for further analysis and evaluation in the remainder of this study.

Based on the previous analysis, and within the same framework of the 16-electrode configuration, both commonly used patterns AD, SK, and OP (cf figure 3) as well as the newly proposed RR (cf figure 4) are compared using the FE model. The current density integral J_L for the lungs as defined in equation (9) is calculated to analyze the previously mentioned patterns.

Figure 10 displays results for the healthy lung case. It depicts the aggregated lung current densities against the index of the current injection electrodes for the four injection patterns and a current streamline plot in the electrode plane for the OP pattern. We observe that the OP pattern exhibits higher values across various injection indices than AD and SK. The OP pattern is followed closely by the proposed pattern RR. The highest density is registered between electrodes 7–15 in the 7th injection of the OP pattern. We observe wide current streamline coverage across the thorax. A critical observation concerns the number of distinct current paths, which is 28 for the proposed RR pattern, and thus higher than for the classical patterns, while

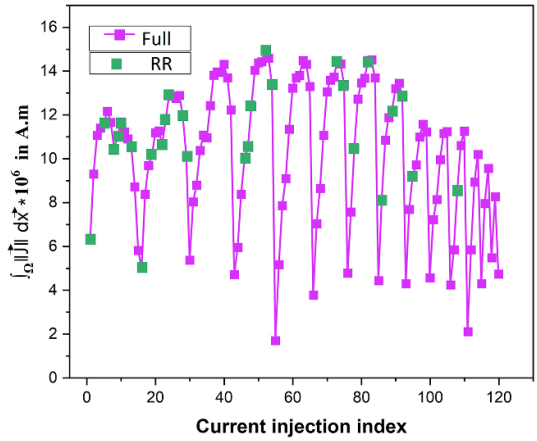

Figure 8. Comparison of current density between RR and Full patterns for healthy lungs. The RR pattern, using only 8 electrodes, shows close current density trends as the Full pattern, which uses 16 electrodes, indicating its efficiency with fewer injections.

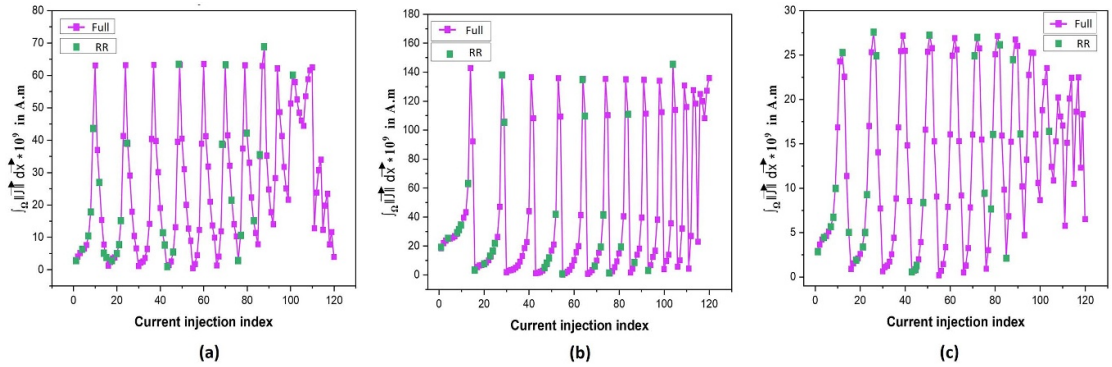

Figure 9. Comparison of current density within the lung nodule between RR and full patterns for (a) case 1, (b) case 2, and (c) case 3.

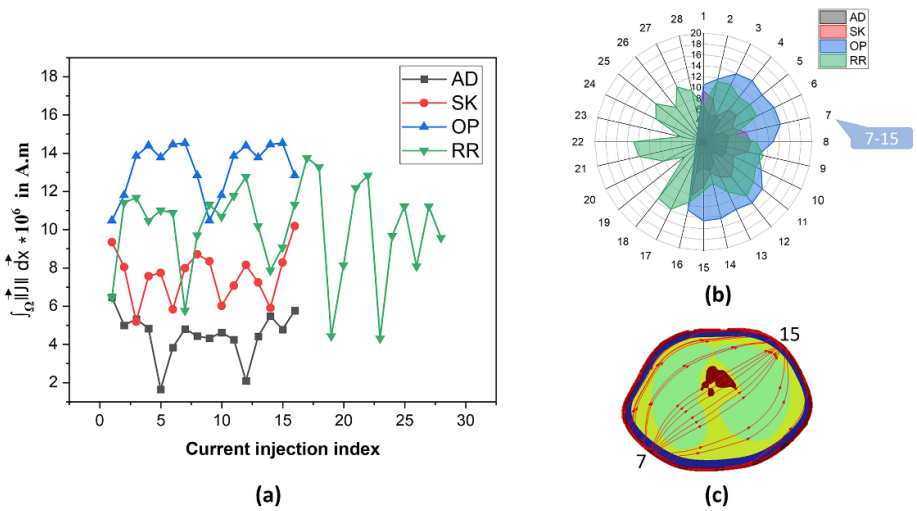

Figure 10. (a) Evaluation of the current density within the healthy lungs for the AD, OP, SK, and RR patterns, (b) radar plot of the current density within the healthy lungs, (c) cross-section streamlines presenting the highest current density index within the pair of electrodes 7–15 using OP pattern.

employing only 8 electrodes. Notably, the 17th RR injection, traversing electrodes 5–13, demonstrated the highest density. This comparative analysis is conducted in a second step on three distinct positions of nodules within the lungs as shown in figure 11. The calculation of current density integral in the lungs considers their inhomogeneous composition influenced by nodule tissue in cases 1, 2, and 3. Figure 11

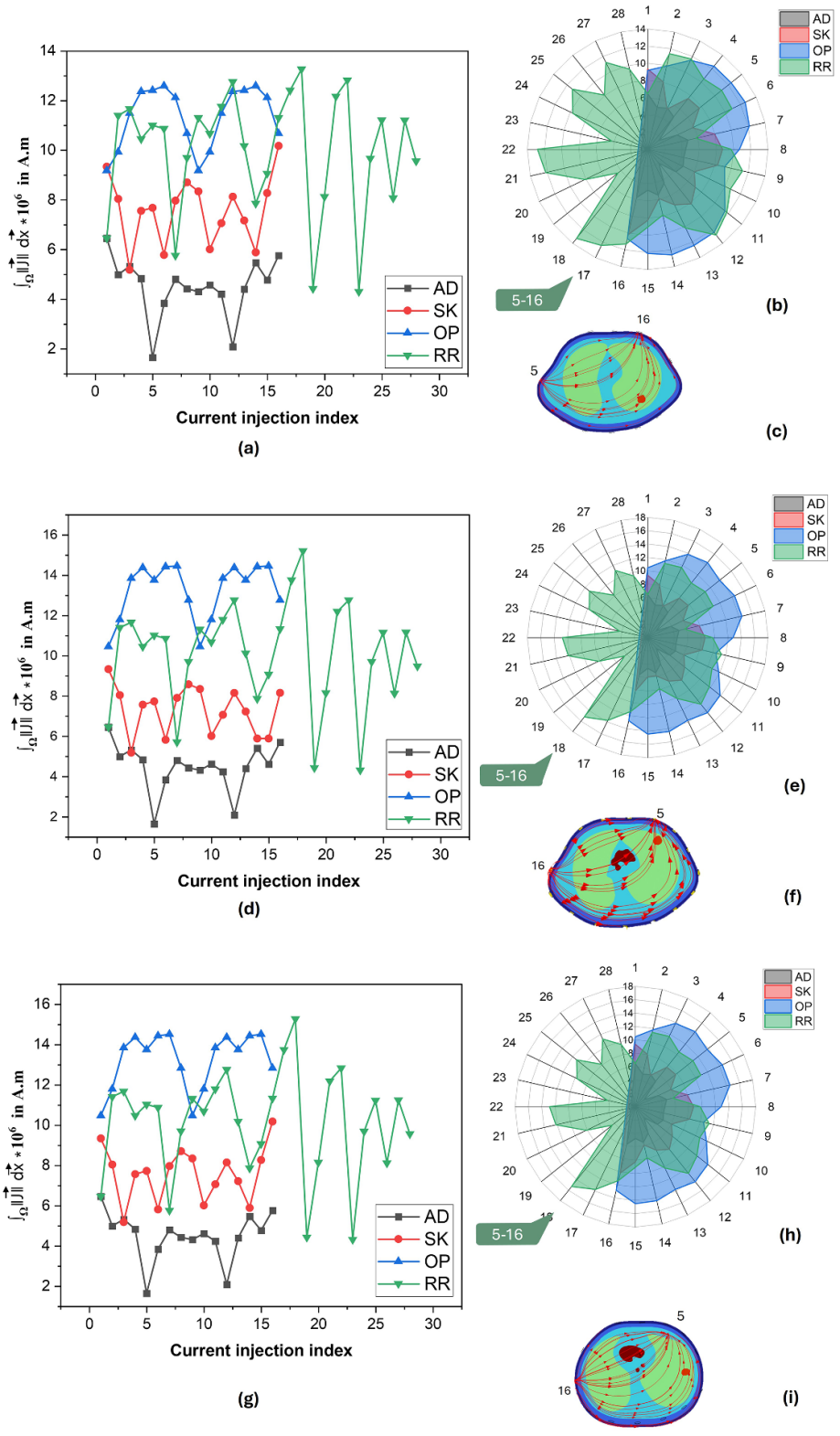

Figure 11. (a), (d) and (g) Evaluation of the current density within the unhealthy lungs for the AD, OP, SK, and RR patterns for the 3 nodule positions, (b), (e) and (h) radar plots of the current density within the unhealthy lungs, (c), (f) and (i) cross-section of the three FEM models indicating the position of the nodule to the highest injection indices.

illustrates the resulting density within the whole lung volume including the nodule by varying its position. The RR pattern shows higher values for the lungs even with an inhomogeneous composition, followed by OP, SK, then AD. The current density results show that the higher density is located between electrodes 5–16 for the three cases using the RR pattern, with a variation of the integral amplitude. The current density for case 1 reached $6.45 \cdot 10^{-6}$ A m, $10.17 \cdot 10^{-6}$ A m, $12.59 \cdot 10^{-6}$ A m, and $13.27 \cdot 10^{-6}$ A m, for the AD, SK, OP, and RR patterns, respectively. The results demonstrate that the RR pattern yields a higher maximum peak

value for the unhealthy lung case 1 compared to the OP pattern, which had previously exhibited superior performance for the healthy lung. For nodule case 2, the current density registered peaks of $6.44 \cdot 10^{-6}$ A m, $9.32 \cdot 10^{-6}$ A m, $14.45 \cdot 10^{-6}$ A m, and $15.20 \cdot 10^{-6}$ A m, for the AD, SK, OP, and RR patterns respectively, leading to the effectiveness of diffusing more current into the lung case 2 using the RR pattern. The same critical evaluation goes to case 3, where the current attains peaks of $6.46 \cdot 10^{-6}$ A m, $10.17 \cdot 10^{-6}$ A m, $14.51 \cdot 10^{-6}$ A m, and $15.27 \cdot 10^{-6}$ A m, for the patterns AD, SK, OP, and RR respectively.

In the next step, the current density of the nodule is studied to investigate the advantages of using the proposed pattern as shown in figure 12. Analysis shows that RR exhibits better performance with higher peaks of aggregated current within the nodule compared to the surrounding tissues in three different positions. For case 1, $72.73 \cdot 10^{-9}$ A m is registered between electrodes 13–10 using the RR pattern, which is the nearest current path to the nodule in the first position representing a sign of detecting changes in the current amplitude driven through the inserted nodule. As for case 2, electrodes pair 13-16 exhibits the highest value of $145.24 \cdot 10^{-9}$ A m applying RR followed by SK, then OP. Finally, $26.43 \cdot 10^{-9}$ A m is reached for case 3 between electrodes 2–13 applying the RR pattern. A critical analysis of the nodule cases is that the AD patterns show the lowest current density values, confirming that they tend to drive current mainly along the boundaries rather than the interior regions of the lungs. The second study evaluates the sensitivity of the measured electrical potential within the electrodes to the anomaly integration into the healthy lung model. The electrical potential measurements between different pairs of electrodes in the lung models are shown in figure 13. The measurements, plotted against the measurement index, compare the electrical potential difference resulting from the simulation of the common injection patterns compared to the proposed pattern between the healthy lung and the lung with nodules. The nodule position is highlighted in figures 2 and 7. Figure 13(a) shows a difference in electrical potentials for nodule case 1, with the proposed pattern RR consistently higher than AD, SK, and OP, reaching 0.035V as a potential difference. Figure 13(b) shows higher potential values in RR and OP patterns, for the nodule in case 2. Figure 13(c) illustrates the nodule in case 3, where the RR pattern shows higher electrical potential in one measurement index than the common patterns, reaching 0.038 V as a potential difference. The AD pattern maintains lower values in the three cases. These differences in electrical potential highlight the sensitivity of specific electrode configurations in detecting lung nodules, suggesting potential diagnostic applications.

4.2. Sensitivity of the current injection patterns to changes in the nodule position

The sensitivity of an EIT injection represents the expected change in simulated current density for changes in the nodule position. A selection of the electrode index showing the highest current density is made to be considered as the highest sensitive region of every injection round of the examined patterns since it is informative about the nodule position. This study relies on analyzing the abilities of EIT patterns to distinguish changes in the position of internal structures. In this context, the sensitivity indicator is denoted by S, and calculated as

$$S_p^{1,2} = \frac{\triangle J_p^{1,2}}{d^{1,2}} = \frac{|J_{A_2} - J_{A_1}|}{\|\vec{x}_2 - \vec{x}_1\|} \tag{11a}$$

$$[2ex]\, S_p^{2,3} = \frac{\triangle J_p^{2,3}}{d^{2,3}} = \frac{|J_{A_3} - J_{A_2}|}{\|\vec{x}_3 - \vec{x}_2\|} \tag{11b}$$

$$[2ex]\, S_p^{3,1} = \frac{\triangle J_p^{3,1}}{d^{3,1}} = \frac{|J_{A_1} - J_{A_3}|}{\|\vec{x}_1 - \vec{x}_3\|} \tag{11c}$$

where $\triangle J_p^{1,2}$, $\triangle J_p^{2,3}$, and $\triangle J_p^{3,1}$ is the variation of the calculated current density between cases 1 and 2, cases 2 and 3, and cases 3 and 1 respectively within the highest indices, for each pattern $p \in \{\text{AD, OP, SK, Full, RR}\}$, and $J_{A_i}, i = 1, 2, 3$, denotes the integrated current density strength for the ith location of the anomaly (cf equation (9)). The (centroid) positions of the nodule in cases 1, 2, and 3 are $\vec{x}_1$, $\vec{x}_2$ and $\vec{x}_3$, respectively. The resulting sensitivity indicators of the four different patterns are given in table 5 and show that the values are highest for the proposed RR pattern, with values of $7.79 \cdot 10^{-7}$ A, $10.5 \cdot 10^{-7}$ A, $3.88 \cdot 10^{-7}$ A, for $S^{1,2}$, $S^{2,3}$, and $S^{3,1}$ respectively, compared to AD, SK, and OP. In addition, results show that the RR is conserving the high sensitivity reached by using the Full set of electrodes as previously highlighted in figures 8 and 9. The sensitivity to changes from case 2 to case 3 exhibits the highest values for the different patterns compared to the sensitivity between the rest of the cases. The OP pattern showed the minimum sensitivity $S^{1,2}$, and $S^{3,1}$ due to the low current density for case 1, since the nodule, in that case, is placed near the electrodes, which makes the AD, followed by SK favorable patterns for the detection and current density. These findings demonstrate that the RR and SK patterns are more effective at capturing anomaly changes, confirming that the current penetration is increased within the human thorax tissues by skipping more electrodes. The

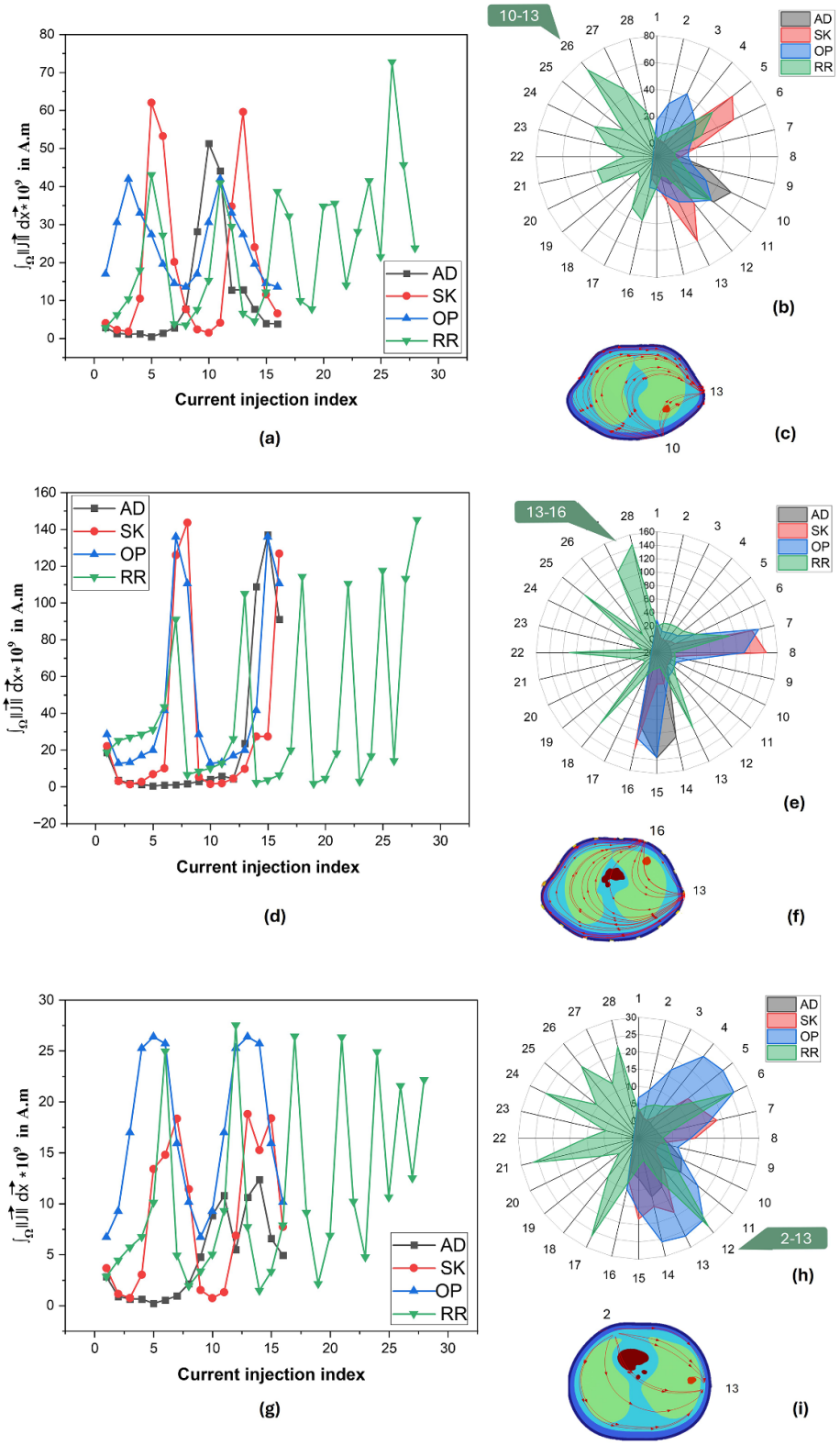

Figure 12. (a), (d) and (g) Evaluation of the current density within the lung nodule for the AD, OP, SK, and RR patterns for the 3 cases, (b), (e) and (h) radar plots of the current density within the lung nodules, (c), (f) and (i) cross-section of the three FEM models indicating the position of the nodule to the highest injection indices.

differences in sensitivity between the patterns highlight the importance of carefully selecting the electrode configuration to optimize the performance of the EIT system for nodule detection. The present study provides valuable insight into the efficacy of the FE model quality for reliable investigations, compared to the models highlighted in table 1. In addition, this comprehensive approach ensures that the novel injection pattern is effectively validated compared to the common injection patterns by reaching maximal current density and sensitivity to anomaly changes.

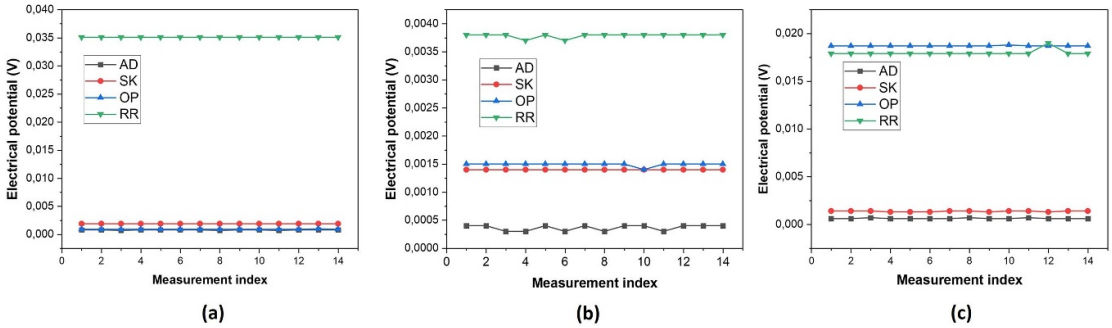

Figure 13. Comparison of electrical potential differences in healthy lung and lung with nodules under various current injection patterns: (a) electrical potential difference for nodule case 1, (b) electrical potential difference for nodule case 2, (c) electrical potential difference for nodule case 3.

Table 5. Sensitivity of the current injection patterns over changes in lung nodule position (in 10^{-7} A).

Pattern	AD	SK	OP	Full	RR
$S^{1,2}$	7.10	6.76	6.01	7.79	**7.79**
$S^{2,3}$	9.98	9.56	9.75	10.5	**10.5**
$S^{3,1}$	3.34	3.61	1.33	3.88	**3.88**

5. Conclusion and perspectives

In this paper, the current injection patterns for human thorax EIT are investigated, and a novel injection pattern is proposed. To evaluate the common injection patterns to the proposed one, a FEM model that closely mimics the real shape and dielectric properties of the human body, including the insertion of lung nodules in three different positions, was developed. Mesh assessment is considered a crucial step, as it is essential for reliable EIT calculations. A convergence study of the mesh within the lungs and the inserted cancer tissue was then conducted to determine the optimal mesh elements suitable for FEA calculations.

For quantitative evaluation of the proposed injection pattern, we compare the RR pattern to the common patterns based on the current density within the lung nodules in the three different positions, the electrical potential measured within the electrodes, in addition to the sensitivity to the anomaly position change. The proposed pattern was aimed to minimize the number of electrodes while gaining more information. Analysis showed that the elaborated pattern has the maximum current density compared to the common patterns of the lung nodule. The FE analysis showed magnitudes of $72.73 \cdot 10^{-9}$ A · m, $145.24 \cdot 10^{-9}$ A · m, and $26.43 \cdot 10^{-9}$ A · m for positions 1, 2, and 3, respectively, using RR pattern. Furthermore, the impact of nodule position changes on the current density for different patterns was assessed through sensitivity analysis. The results demonstrated that the RR pattern remained the most effective, even with variations in nodule location, with a sensitivity of $7.79 \cdot 10^{-7}$ A, $10.5 \cdot 10^{-7}$ A,$1.33 \cdot 10^{-7}$ A, for $S^{1,2}$, $S^{2,3}$, and $S^{3,1}$ respectively.

This study provides valuable insights into the optimization of current injection patterns for lung monitoring using EIT, with the proposed RR pattern demonstrating promising results in terms of current density and sensitivity to nodule position. Ongoing research aims to further enhance the performance and clinical applicability of EIT for lung imaging and nodule detection. As a perspective for future work, the proposed pattern will be integrated into the EIT measurement system to gain a better understanding and analysis.

Data availability statement

All data that support the findings of this study are included within the article (and any supplementary information files).

Acknowledgments

This research has been supported by the Project EmbodiedTech (57681375) funded by the German Academic Exchange Service (DAAD). It has also been supported by the Ministry of Higher Education and Scientific Research of Tunisia in granting an additional research stay in Germany, in 2023.

ORCID iDs

Oumaima Bader https://orcid.org/0000-0002-1579-1787
Oliver G Ernst https://orcid.org/0000-0002-0176-7321
Olfa Kanoun https://orcid.org/0000-0002-7166-1266

References

Adler A, Gaggero P O and Maimaitijiang Y 2011 Adjacent stimulation and measurement patterns considered harmful *Physiol. Meas.* **32** 731–44
Adler A and Holder D 2021 *Electrical Impedance Tomography: Methods, History and Applications* (CRC Press)
Al-Abassi A, Papini M and Towler M 2022 Review of biomechanical studies and finite element modeling of sternal closure using bio-active adhesives *Bioengineering* **9** 198
Avis N J and Barber D C 1994 Image reconstruction using non-adjacent drive configuration *Physiol. Meas.* **16** A153–60
Bader O, Essoukri Ben Amara N and Kanoun O 2022 Realistic 2D model of the human thorax for electrical impedance tomography *2022 Int. Workshop on Impedance Spectroscopy (IWIS)* (IEEE) pp 70–74
Bader O, Hafsa M, Essoukri Ben Amara N and Kanoun O 2021 Two-dimensional forward modeling for human thorax imaging based on electrical impedance tomography *2021 Int. Workshop on Impedance Spectroscopy (IWIS)* (IEEE) pp 114–7
Borcea L 2002 Electrical impedance tomography *Inverse Problems* **18** R99
Brown B H and Seagar A D 1987 The Sheffield data collection system *Clin. Phys. Physiol. Meas.* **8** 91–97
COMSOL Multiphysics 2024 *Mesh Element Quality and Size* (available at: https://doc.comsol.com/5.5/doc/com.comsol.help.comsol/comsol_ref_mesh.15.18.html) (Accessed 25 July 2024)
Dang C, Bellis C, Darnajou M, Ricciardi G, Mylvaganam S and Bourennane S 2021 Practical comparisons of EIT excitation protocols with applications in high-contrast imaging *Meas. Sci. Technol.* **32** 085110
Demidenko E, Hartov A, Soni N and Paulsen K D 2005 On optimal current patterns for electrical impedance tomography *IEEE Trans. Biomed. Eng.* **52** 238–48
Dussel N, Fuchs R, Reske A W and Neumuth T 2022 Automated 3D thorax model generation using handheld video-footage *Int. J. Comput. Assist. Radiol. Surg.* **17** 1707–16
Fan W R and Wang H X 2010 3D modelling of the human thorax for ventilation distribution measured through electrical impedance tomography *Meas. Sci. Technol.* **21** 115801
Fedorov A *et al* 2012 3D slicer as an image computing platform for the quantitative imaging network *Magn. Reson. Imaging* **30** 1323–41
Haddad H, Bader O, Hafsa M, Essoukri Ben Amara N and Kanoun O 2021 Forward modelling of the human thorax for electrical impedance tomography measurements *2021 Int. Workshop on Impedance Spectroscopy (IWIS)* (IEEE) pp 126–30
Huang N, Ma Y, Zhang M, Ge H and Wu H 2021 Finite element modeling of human thorax based on MRI images for EIT image reconstruction *J. Shanghai Jiaotong Univ.* **26** 33–39
Kauppinen P, Hyttinen J and Malmivuo J 2006 Sensitivity distribution visualizations of impedance tomography measurement strategies *Int. J. Bioelectromagn.* **8** 63–71 (available at: www.bem.fi/book/26/ijbem/volume8/number1/htm/kauppine.htm)
Lee M, Paul A, Xu Y, Hairston W and Cauwenberghs G 2022 Characterization of Ag/AgCl dry electrodes for wearable electrophysiological sensing *Front. Electron.* **2** 700363
Li X, Chen X, Wang Q, Wang J, Duan X, Sun Y and Wang H 2019 Electrical-impedance-tomography imaging based on a new three-dimensional thorax model for assessing the extent of lung injury *AIP Adv.* **9** 125310
Lionheart W R B, Kaipio J and McLeod C N 2001 Generalized optimal current patterns and electrical safety in EIT *Physiol. Meas.* **22** 85
Ma M, Hao Z, Wang Q, Li X, Duan X, Wang J and Feng H 2023 3-D electrical impedance imaging of lung injury *Prog. Electromagn. Res.* B **103** 19–36
Malvezzi M, Carioli G, Bertuccio P, Boffetta P, Levi F, La Vecchia C and Negri E 2019 European cancer mortality predictions for the year 2019 with focus on breast cancer *Ann. Oncol.* **30** 781–7
MedDream 2024 *DICOM Library* (available at: www.dicomlibrary.com) (Accessed 25 July 2024)
Menden T, Orschulik J, Slimi M, Leonhardt S and Walter M 2018 Development of an electrical phantom for multi-frequency electrical impedance tomography based on the visible human project *Int. J. Bioelectromagn.* **20** 51–54
Putensen C, Hentze B, Muenster S and Muders T 2019 Electrical impedance tomography for cardio-pulmonary monitoring *J. Clin. Med.* **8** 1176
Rapin M, Braun F, Adler A, Wacker J, Frerichs I, Vogt B and Chetelat O 2018 Wearable sensors for frequency-multiplexed EIT and multilead ECG data acquisition *IEEE Trans. Biomed. Eng.* **66** 810–20
Somersalo E, Cheney M and Isaacson D 1992 Existence and uniqueness for electrode models for electric current computed tomography *SIAM J. Appl. Math.* **52** 1023–40
Tomicic V and Cornejo R 2019 Lung monitoring with electrical impedance tomography: technical considerations and clinical applications *J. Thorac. Dis.* **11** 3122
Wang Y, Yue S, Chen J and Li Q 2022 Conductivity characteristics of human lung tissues *Int. J. Imaging Syst. Technol.* **32** 178–91
Wu H, Xu G, Zhang S, Yang S, Li Y and Yan W 2006 Forward problem of three dimensional EIT in thorax model *2006 Int. Conf. IEEE Engineering in Medicine and Biology Society* (IEEE) pp 6627–30
Zhang L and Wang H 2010 Single source current drive patterns for electrical impedance tomography *Proc. Conf. Instrumentation and Measurement Technology (Austin, TX)* (IEEE) pp 1477–80
Zhang T, Jang G Y, Kim Y E, Oh T I, Wi H and Woo E J 2020 Influence of current injection scheme on electrical impedance tomography for monitoring of the respiratory function of obese subjects *J. Appl. Phys.* **128** 174902
Zhou L, Harrach B and Seo J K 2018 Monotonicity-based electrical impedance tomography for lung imaging *Inverse Problems* **34** 045005